Dalton Transactions

ROYAL SOCIETY OF CHEMISTRY

PAPER

View Article Online
View Journal | View Issue

Cite this: *Dalton Trans.*, 2026, **55**, 3276

An iron-based organic framework-modified Cu–Co–Fe ternary layered double hydroxide enhanced adsorptive removal of antibiotics

Zhuo Han,[a,b] Haofeng Wu,[b] Ge Niu,[b] Baichuan Tang,[b] Zhongyi Zhao,[b] Minmeng Tang,[b] Linhua Zhu,[c] Yanhong Chao,*[c,d] Wenshuai Zhu *[b] and Yuanbin She *[a]

Adsorption has emerged as a green and promising solution for antibiotic removal in wastewater treatment systems, driving an urgent demand for designing high-performance and eco-friendly adsorbents that enable rapid and efficient elimination of antibiotic contaminants. Herein, a high-activity Fe-based metal–organic framework (Fe-MOF) was *in situ* integrated with a copper–cobalt–iron layered double hydroxide (CuCoFe-LDH) *via* a two-step hydrothermal synthesis process, successfully fabricating an engineered Fe-MOF@CuCoFe-LDH composite adsorbent that exhibits significantly enhanced adsorption capacity and broad applicability. The Fe-MOF nanospheres were uniformly hybridized into the two-dimensional nanocluster flakes of the ternary hydrotalcite CuCoFe-LDH, forming a hierarchical heterostructure. This synergistic configuration substantially boosted the density of active surface sites on the LDH-based adsorbent, resulting in significantly improved adsorption kinetics along with enhanced adsorbate-binding capacity. The removal efficiency of the tetracycline antibiotic (TC) by the as-prepared Fe-MOF@CuCoFe-LDH composite reaches 94.8%, even at a high initial TC concentration of 300 mg L^{-1}, which represents a 36.7% and 9.4% increase compared to that of pristine Fe-MOF and CuCoFe-LDH, respectively. A high Langmuir maximum adsorption capacity of 2500 mg g^{-1} was achieved. The adsorption mechanism was speculated to involve metal complexation, metal–π, H-bonding and electrostatic interactions as well as hydrophobic interactions. In addition, the Fe-MOF@CuCoFe-LDH composite demonstrated exceptional cycling stability, retaining 97.8% TC removal efficiency for five adsorption–desorption cycles, highlighting its outstanding adaptability and promising potential for practical wastewater remediation applications.

Received 23rd October 2025,
Accepted 13th January 2026

DOI: 10.1039/d5dt02540k

rsc.li/dalton

1. Introduction

The ubiquitous presence of and constant exposure to numerous antibiotics in the aquatic environment have raised a significant concern over the harmful effects they have on the ecosystem balance and human health. With the increasing use of antibiotics in human medicine, agriculture, and aquaculture, the threat of the accumulation of antibiotics in natural water bodies is also on the rise. To overcome this challenge, there is a need to put in place concrete intervention measures such as enhanced wastewater treatment technologies, sound regulatory measures, and enhanced awareness among the population. An interdisciplinary approach that would comprise environmental science, public health, policymaking, and technology innovation is the key to mitigating the adverse impact of antibiotic pollution and safeguarding the quality of water.

At present, the adsorption method is regarded as a highly efficient treatment strategy, owing to its operational simplicity, cost-effectiveness, robust performance, and absence of secondary pollutants.[1–4] Adsorption operates as a non-destructive removal process that relies on the interaction between pollutants and adsorbent materials, either chemically or physically, to separate and eliminate antibiotics.[5] The implementation of adsorption techniques has spurred the development of a wide range of innovative adsorbent materials, including various soils,[6] polymers,[7] activated carbon,[8] clay minerals,[9] carbon nanotubes,[10] aerogel,[11] metal–organic frameworks,[12] biochar,[13] molybdenum disulfide,[14] graphene quantum

[a]*College of Chemical Engineering, State Key Laboratory of Green Chemical Synthesis and Conversion, Zhejiang University of Technology, Hangzhou, Zhejiang 310014, P. R. China. E-mail: sheyb@zjut.edu.cn*
[b]*College of Chemical Engineering and Environment, State Key Laboratory of Heavy Oil Processing, China University of Petroleum-Beijing, Beijing 102249, P.R. China. E-mail: zhuws@cup.edu.cn*
[c]*The International Joint Research Center for Clean and Efficient Utilization of Hydrocarbon Resources in the South China Sea of Hainan Province, Key Laboratory of Water Pollution Treatment and Resource Reuse of Hainan Province, Hainan Normal University, Haikou 571158, P.R. China. E-mail: chaoyh@cup.edu.cn*
[d]*College of Science, China University of Petroleum-Beijing, Beijing 102249, P.R. China*

dots,[15] boron nitride,[16] *etc*. Among these materials, two-dimensional nanosheets emerge as premier candidates, capitalizing on their ultrahigh specific surface area, engineerable surface architectures, and abundant exposed reactive centers, collectively enabling exceptional adsorption performance.

The distinct chemical composition of layered double hydroxides (LDHs) imparts unique characteristics to them,[17] including the ability to swap anions,[18] variability of component metal elements,[19] regulation of basicity,[20] and exhibition of memory function.[21] Controlled calcination of hydrotalcite (CLDH) yields highly reactive layered double oxides (LDOs) or mixed metal oxides (MMOs), significantly enhancing the material's functional utility.[22] The structural versatility of LDH and its derived LDOs and MMOs drives their multidisciplinary applicability, including adsorption processes, photo(electro) catalytic systems, pharmaceutical formulations, flame-retardant materials, and related advanced technologies.[23] LDHs, with large lamellar structures, enhance pollutant adsorption by offering interlayer exchangeable anions and adjustable host layer properties. Adsorption of PFAS on hydrotalcite (HT), an LDH, was achieved through a combination of ion exchange, hydrophobic interactions, and electrostatic attraction according to Kim *et al.*, who used reaction solutions containing PFAS concentrations relevant to the environment. However, the relative importance of these three mechanisms warrants additional investigation.[24] The highest adsorption capacity of 279.23 mg g^{-1} was achieved by Sara Samuel *et al.* through the synthesis of MgFe-LDH, which was specifically designed to target the removal of Reactive Red 43 dye.[25] In another study, Tian *et al.* found that ZnCoCr-LDHs exhibited superior fluoride adsorption efficiency compared to both Zn-LDHs and ZnCo-LDHs. The improved performance was linked to the incorporation of Cr^{3+} ions, which enhanced the materials' fluoride ion uptake.[26] Meanwhile, Lu *et al.* achieved a theoretical highest capacity of adsorption of 1688.22 mg g^{-1} for methyl orange (MO) using MgFe-LDH under optimized synthesis conditions. Their analysis attributed this high adsorption potential to an electrostatic combination interaction, hydrogen bonding, complex formation, and ion exchange processes.[27]

Metal–organic frameworks (MOFs) have emerged as premier nanomaterials in materials science, characterized by ultrahigh surface areas, tunable pore volumes, uniform pore architectures, and exceptional thermal resilience. Gai *et al.* synthesized two types of three-dimensional zinc-based MOFs and their flexible composites through a solvothermal method conducted at normal temperature. These newly developed MOFs demonstrated excellent antibiotic removal efficiency in aqueous solutions, attributed to their porous networks and rich functional group content.[28] The integration of PTA enhanced the composite's electronegativity, which significantly improved its adsorption of cationic antibiotics *via* π–π stacking and electrostatic interactions.[29] Among various MOFs, Fe-based materials are particularly attractive due to their environmental stability and low toxicity, which positions them as suitable candidates for environmental and biomedical uses.[30] For instance, Yang *et al.* prepared Fe-BTC to effectively adsorb perfluorooctanoic acid (PFOA) from water.[31] Njaramba *et al.* designed a mixed matrix membrane (MMM) comprising an Fe-MOF and polyvinylidene fluoride (PVDF), further functionalized with β-cyclodextrin (β-CD), to improve the aqueous extraction of ciprofloxacin (CIP).[32] Wang *et al.* engineered an Al^{3+} modified Fe-MOF (Al@Fe-MOF) *via in-situ* synthesis to improve the selenite (Se(IV)) adsorption performance.[33] These advancements suggest that Fe-MOFs, due to their structural and functional properties, hold strong potential for antibiotic adsorption in wastewater treatment.

In this study, an Fe-MOF hybrid-modified two-dimensional ternary CuCoFe-LDH composite, referred to as Fe-MOF@CuCoFe-LDH, was synthesized using a two-step hydrothermal method and applied for enhanced adsorptive removal of the antibiotic tetracycline (TC). Notably, the hybridization of the Fe-MOF with ternary CuCoFe-LDH will be rationally designed based on their complementary advantages: the Fe-MOF can provide an ultrahigh specific surface area and well-defined porosity to facilitate TC mass transfer, while the ternary CuCoFe-LDH will offer abundant mixed metal active sites (Fe, Cu, and Co) for enhanced coordination with TC's functional groups (–OH and $–CONH_2$). The synergistic effect of multiple metals,[34] which couples the heterogeneous dispersion and hybridization effect between the Fe-MOF and CuCoFe-LDH, is expected to effectively facilitate the availability of abundant adsorption active sites of the composite. Additionally, advanced synthesis strategies like the green solvent-induced crystallization of CD-MOFs highlight the feasibility of eco-friendly synthesis,[35] while our two-step hydrothermal approach can ensure structural integrity of the hierarchical heterostructure at relatively lower temperatures. Recent studies on MOF/LDH composite membranes and multi-metal interactions for pollutant disposal further support the efficacy of MOF-LDH hybridization in environmental remediation.[36–38]

Herein, the engineered composite of Fe-MOF@CuCoFe-LDH is proposed to synergistically improve the adsorption performance for the antibiotic tetracycline (TC). Kinetic, thermodynamic, and isotherm analyses were used to investigate the behavior of the adsorption. The stability of the composite during several adsorption–desorption cycles and under different pH conditions was investigated in detail. Additionally, the adsorption mechanisms were also discussed based on the experimental results.

2. Experimental section

2.1 Materials and reagents

Tetracycline (TC, ≥95.0% purity), hexamethylenetetramine ($C_6H_{12}N_4$), and trimesic acid ($C_6H_3(CO_2H)_3$) were obtained from Sigma-Aldrich. Other chemicals including cupric nitrate nonahydrate ($Cu(NO_3)_2{\cdot}6H_2O$), cobaltous nitrate nonahydrate ($Co(NO_3)_2{\cdot}6H_2O$), ferric nitrate nonahydrate ($Fe(NO_3)_3{\cdot}9H_2O$), ferric chloride ($FeCl_3$), *N*,*N*-dimethylformamide (C_3H_7NO), hydrochloric acid (HCl), sodium hydroxide (NaOH), ethylene

glycol and ethanol were of analytical grade and purchased from Sinopharm Chemical Reagent Co., Ltd. Ultra-pure water was used throughout the experiment and the working solution was freshly prepared.

2.2 Characterization

The surface morphologies of the synthesized materials were examined using a JSM-7001F field emission scanning electron microscope (SEM). X-ray photoelectron spectroscopy (XPS) was performed on a Thermo Scientific VG MultiLab 2000 spectrometer to determine the elemental composition of the materials. X-ray diffraction (XRD) analysis was performed using a Shimadzu XRD-6100Lab instrument with Cu K_α radiation (λ = 0.15406 nm) and a nickel filter to determine the materials' crystallinity, phase structure, and crystallite size. Data collection spanned scattering angles (2θ) from 10° to 80° with a 4° step size. Fourier-transform infrared spectroscopy (FT-IR) spectra were recorded using a Nicolet Nexus 470 in the range of 400 to 4000 cm^{-1}.

2.3 Synthesis of the Fe-MOF

To prepare the Fe-MOF, ferric chloride (51.9 mg) was dissolved in 20 mL of ethylene glycol and stirred until complete dissolution to obtain Solution A. Trimesic acid (76.6 mg) was dissolved in 20 mL of *N*,*N*-dimethylformamide and stirred until fully dissolved to yield Solution B. Subsequently, Solution A and Solution B were mixed and stirred for 1 h, followed by transfer into a 100 mL stainless steel autoclave to react at 120 °C for 24 h. The product was then dried in an oven at 80 °C for 12 h to yield a fine reddish-brown powder, which was identified as the Fe-MOF. This powder was kept carefully to ensure that it does not get wet.

2.4 Synthesis of the Fe-MOF@CuCoFe-LDH composite

The composite of Fe-MOF@CuCoFe-LDH nanoarchitectures was constructed through an *in situ* hydrothermal co-precipitation method. Specifically, a certain amount of the Fe-MOF was homogeneously dispersed in 40 mL of deionized water using sonication. Subsequently, $Co(NO_3)_2{\cdot}6H_2O$, $Cu(NO_3)_2{\cdot}9H_2O$, $Fe(NO_3)_3{\cdot}9H_2O$, and $C_6H_{12}N_4$ were added to the Fe-MOF suspension solution at a molar ratio of 1 : 1 : 1 : 1.3. The homogeneous suspension underwent hydrothermal treatment in a 100 mL Teflon-lined stainless steel autoclave at 120 °C for 24 h. After natural cooling to room temperature, the precipitate was washed three times with ethanol to remove impurities, vacuum-dried at 80 °C, and designated as Fe-MOF@CuCoFe-LDH. To make a comparison, a similar material (CuCoFe-LDH) was also prepared, without the Fe-MOF.

This process produced a new material with the high surface area of the Fe-MOF and the thin sheet-like morphology of CuCoFe-LDH. The application of sound waves facilitated the dispersion of the Fe-MOF particles to distribute them uniformly, enabling the other material to grow around them easily. As it was heated, the two components were highly bonded together, forming a well-structured material.

Hexamethylenetetramine assisted in regulating the conditions of the process by gradually releasing a base, which maintained the pH and enabled the crystals to grow correctly. The end product was a layered, flaky structure that dispersed with Fe-MOF nanoparticles in it when viewed through a microscope. Such a special structure is quite helpful in adsorbing pollutants in water, as the numerous active sites are exposed and the material becomes stable and reusable in water treatment plants.

2.5 Adsorption experiments

A battery of batch experiments was used to examine the TC adsorption behavior onto Fe-MOF@CuCoFe-LDH. Contact duration, solution pH, adsorbent dosage, temperature, regeneration cycles, adsorbate initial concentration, and other essential operational parameters were fine-tuned to evaluate the material's adsorption performance. Typically, 5 mg of the adsorbent was added to 25 mL of TC aqueous solution at an initial concentration of 300 mg L^{-1} in a conical flask. The flask was wrapped in aluminum foil and shaken at 130 rpm in a constant-temperature water bath maintained at 298 K during the adsorption process. After reaching equilibrium, 5 mL aliquots were aspirated, filtered, and quantified using a UV-2401 spectrophotometer at a wavelength of 358 nm. The material's pH tolerance was evaluated by varying the pH of TC wastewater from 3 to 11, achieved by adding 0.02 mol L^{-1} NaOH or HCl. The capacity of adsorption (eqn (1)) and removal efficiency (%, eqn (2)) were calculated.

$$q_{t,e} = \frac{(C_0 - C_{t,e}) \times V}{m} \quad (1)$$

$$\text{Removal efficiency} = \frac{C_0 - C_e}{C_0} \times 100\% \quad (2)$$

where q_t (mg g^{-1}) and q_e (mg g^{-1}) are, respectively, the adsorption capacity at time t and equilibrium; C_0 (mg L^{-1}), C_t (mg L^{-1}) and C_e (mg L^{-1}) are the TC concentration at initial time, time t and equilibrium, respectively; V (L) is the volume of the liquid employed in the test, and m (g) is the weight of the substance used to adsorb TC. In order to ensure that the results were accurate and reliable, every test was performed thrice under the same conditions, and the average results were considered for analysis.

3 Results and discussion

3.1 XRD analysis

The crystal structures of the samples were analyzed by XRD, and the corresponding patterns of CuCoFe-LDH, Fe-MOF, and Fe-MOF@CuCoFe-LDH are shown in Fig. 1. The hydrothermally synthesized CuCoFe-LDH has characteristic diffraction peaks at 24.14°, 29.61°, and 62.45°, which correspond to the (012), (110) and (214) planes of $Fe(OH)_3$, respectively.[39] The diffraction peaks at 2θ of 36.47° and 42.37° are associated with the (111) and (200) planes of $Co(OH)_2$, respectively.[40]

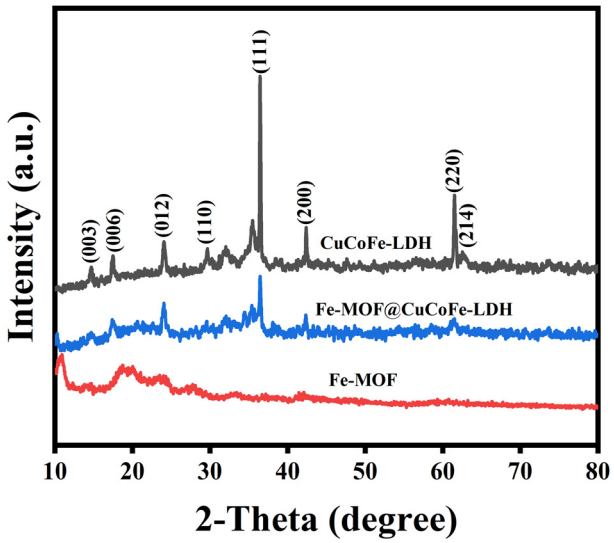

Fig. 1 XRD patterns of CuCoFe-LDH, Fe-MOF, and Fe-MOF@CuCoFe-LDH.

Meanwhile, the peaks located at 2θ of 36.47° and 61.50° correspond, respectively, to the (111) and (220) planes of $Cu(OH)_2$.[64] The typical patterns appeared at 15.25° and 17.89° and are attributed to the (003) and (006) planes of LDH, indicating the successful preparation of the copper–cobalt–iron hydrotalcite. The strong diffraction peak observed at 2θ of 36.47° can be attributed to the coincidence of diffraction peaks from both $Cu(OH)_2$ and $Co(OH)_2$ phases. It is very strong, and the possible reason is that both $Cu(OH)_2$ and $Co(OH)_2$ exhibit diffraction peaks at the same position. For the Fe-MOF sample, a characteristic diffraction peak is observed at 2θ = 10.8°, corresponding to the (100) plane, indicating the formation of the Fe-based MOF structure. After compositing the Fe-MOF with CuCoFe-LDH, the diffraction intensities of the LDH (003) and (006) planes are noticeably weakened. This phenomenon can be attributed to the strong interfacial interaction between Fe-MOF nanospheres and LDH nanosheets, which disrupts the regular layer stacking along the *c* axis and reduces the long-range ordering of the LDH interlayers. Such structural disturbance and partial loss of stacking coherence lead to weakened basal reflections, while the LDH framework remains intact. This result indicates the successful formation of an Fe-MOF@CuCoFe-LDH composite with modified interlayer ordering rather than phase decomposition.

This characterization result is consistent with previous literature reports, confirming the successful preparation of Fe-MOF precursors.[41,42] It may be inferred that the initial location of the characteristic peak in the Fe-MOF@CuCoFe-LDH sample was preserved after the addition of the Fe-MOF, as it was almost identical to that in the CuCoFe-LDH sample. The corresponding peaks in the Fe-MOF@CuCoFe-LDH composite became broader and exhibited reduced intensity. Notably, these microstructural changes (broadening and reduced intensity) indicate a decrease in crystallite size (from ~28 nm for CuCoFe-LDH to ~15 nm for the composite, calculated *via* the Scherrer equation) and an increase in microstrain. Smaller crystallites expose more active sites, while increased microstrain creates additional defects—both effects directly enhance TC adsorption by shortening mass transfer paths and providing more binding sites. The findings of the scanning electron microscopy and infrared characterization were in agreement with this outcome.

3.2 SEM analysis

Fig. 2 presents the scanning electron microscopy (SEM) images of the Fe-MOF, CuCoFe-LDH, and the resulting Fe-MOF@CuCoFe-LDH composite. As shown in Fig. 2a, the pristine Fe-MOF exhibits a typical nanospherical morphology with uniform particle sizes of approximately 100 nm. In contrast, the CuCoFe-LDH sample (Fig. 2b) exhibits an aggregated flake-like or sheet-like structure consisting of irregularly sized two-dimensional nanosheets. Fig. 2c and d reveal a hybrid microstructure after compositing: the Fe-MOF nanospheres are uniformly embedded and dispersed within the matrix of the CuCoFe-LDH nanosheets, forming an integrated hierarchical heterostructure. This intimate interfacial integration between the MOF spheres and LDH flakes contributes to an increased specific surface area and exposes more accessible active sites, which is consistent with the enhanced adsorption performance of the composite.

3.3 FT-IR analysis

The Fourier transform infrared spectra of Fe-MOF, CuCoFe-LDH, and Fe-MOF@CuCoFe-LDH are shown in Fig. 3. For CuCoFe-LDH, a strong, broad absorption peak at 3388 cm^{-1} is attributed to O–H stretching vibrations (from metal hydroxyl groups and hydrogen-bonded water). A strong absorption band at 1357 cm^{-1} arises from red-shifted interlayer CO_3^{2-} ions (compared to free carbonate at 1415 cm^{-1}) due to internal confinement. Prominent peaks at 1385 cm^{-1} and 1533 cm^{-1} correspond to asymmetric stretching of carbonate ions and vibrational modes of nitrate ions, respectively. Absorption bands between 500 cm^{-1} and 800 cm^{-1} are due to M–O–M and M–O–H stretching vibrations. For Fe-MOF@CuCoFe-LDH, all characteristic peaks of CuCoFe-LDH are retained, confirming the preservation of the hydrotalcite structure. Simultaneously, Fe-MOF-specific peaks at 1444 cm^{-1} (C–O stretching of trimesic acid) and 1618 cm^{-1} (aromatic C=C stretching) are observed, with a ~10 cm^{-1} red shift compared to the pristine Fe-MOF (1454 cm^{-1} and 1628 cm^{-1}). Additionally, the O–H stretching peak of CuCoFe-LDH (3388 cm^{-1}) broadens and shifts to 3372 cm^{-1} in the composite. These shifts indicate the formation of hydrogen bonds and coordinate bonds between the Fe-MOF and CuCoFe-LDH, confirming a chemical interaction rather than mere physical mixing. The abundant hydroxyl groups inherited by CuCoFe-LDH facilitate the formation of hydrogen bonds with TC.[43,44] The aromatic ring structure in the Fe-MOF and TC molecules forms π–π stacking, and the hydrophobic regions on the composite surface enhance the affinity for TC. This mechanism aligns with the

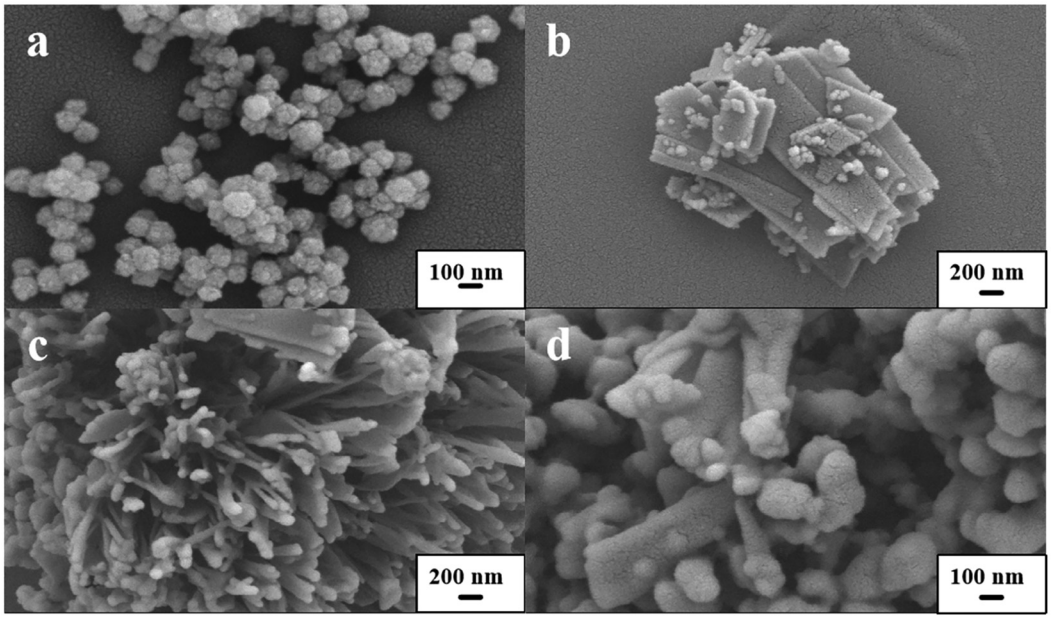

Fig. 2 The SEM images of (a) Fe-MOF, (b) CuCoFe-LDH, and (c and d) Fe-MOF@CuCoFe-LDH.

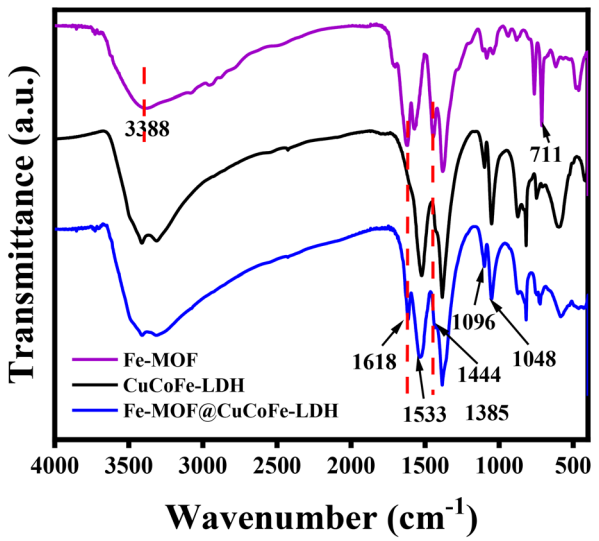

Fig. 3 FT-IR patterns of Fe-MOF, CuCoFe-LDH, and Fe-MOF@CuCoFe-LDH.

research conclusion of Shi *et al.*, where π–π stacking and hydrophobic effects synergistically promote the adsorption of organic pollutants by modified MOF materials.[13,29,45–47]

3.4 XPS analysis

The chemical states and elemental compositions of the surfaces of the CuCoFe-LDH monomer and Fe-MOF@CuCoFe-LDH composites were investigated by XPS characterization. As shown in Fig. 4a, five elements of O, C, Cu, Fe, and Co were detected in both CuCoFe-LDH and Fe-MOF@CuCoFe-LDH.[48] Meanwhile, Fe is predominantly present as Fe^{3+}, as evidenced by the Fe 2p binding energies.[49] As shown in Fig. 4d, the Co 2p spectrum of the composite exhibits two main peaks at 782.08 eV and 798.08 eV, corresponding to Co $2p_{3/2}$and Co $2p_{1/2}$ of Co^{2+}, respectively, accompanied by their satellite peaks at 788.18 eV and 804.18 eV.[40] Similarly, the Cu 2p spectra (Fig. 4c) exhibit characteristic Cu^{2+} signals, indicating that both Cu and Co remain in stable divalent oxidation states after the formation of the composite. Importantly, compared with pristine CuCoFe-LDH, the Fe-MOF@CuCoFe-LDH composite features a well-defined coexistence of Fe^{3+}, Cu^{2+}, and Co^{2+} species on the surface, resulting in abundant multimetallic active sites. These positively charged metal centers can act as Lewis acid sites and readily form coordination interactions with electron-donating functional groups (*e.g.*, –OH and $–CONH_2$) of tetracycline molecules. Such synergistic coordination effects among multiple metal ions significantly enhance the adsorption affinity and stability of the adsorbate–adsorbent complexes. This interpretation is consistent with the findings reported by Mutahir *et al.*, who demonstrated that the MOF-LDH composite adsorbents exhibit superior adsorption performance due to the formation of stable metal–organic complexes between multivalent metal sites and organic pollutants.[47,50]

3.5 Adsorption performance

Fig. 5 shows the comparison of TC adsorption performance on the Fe-MOF, CuCoFe-LDH, and Fe-MOF@CuCoFe-LDH composite. The removal efficiencies of TC by pristine Fe-MOF and CuCoFe-LDH were 60.0% and 85.9%, respectively. In contrast, Fe-MOF@CuCoFe-LDH achieved a significantly higher removal efficiency of 94.8% under the same experimental conditions. This represents an increase of 36.7% and 9.4% compared to that of the Fe-MOF and CuCoFe-LDH, respectively. The Fe-

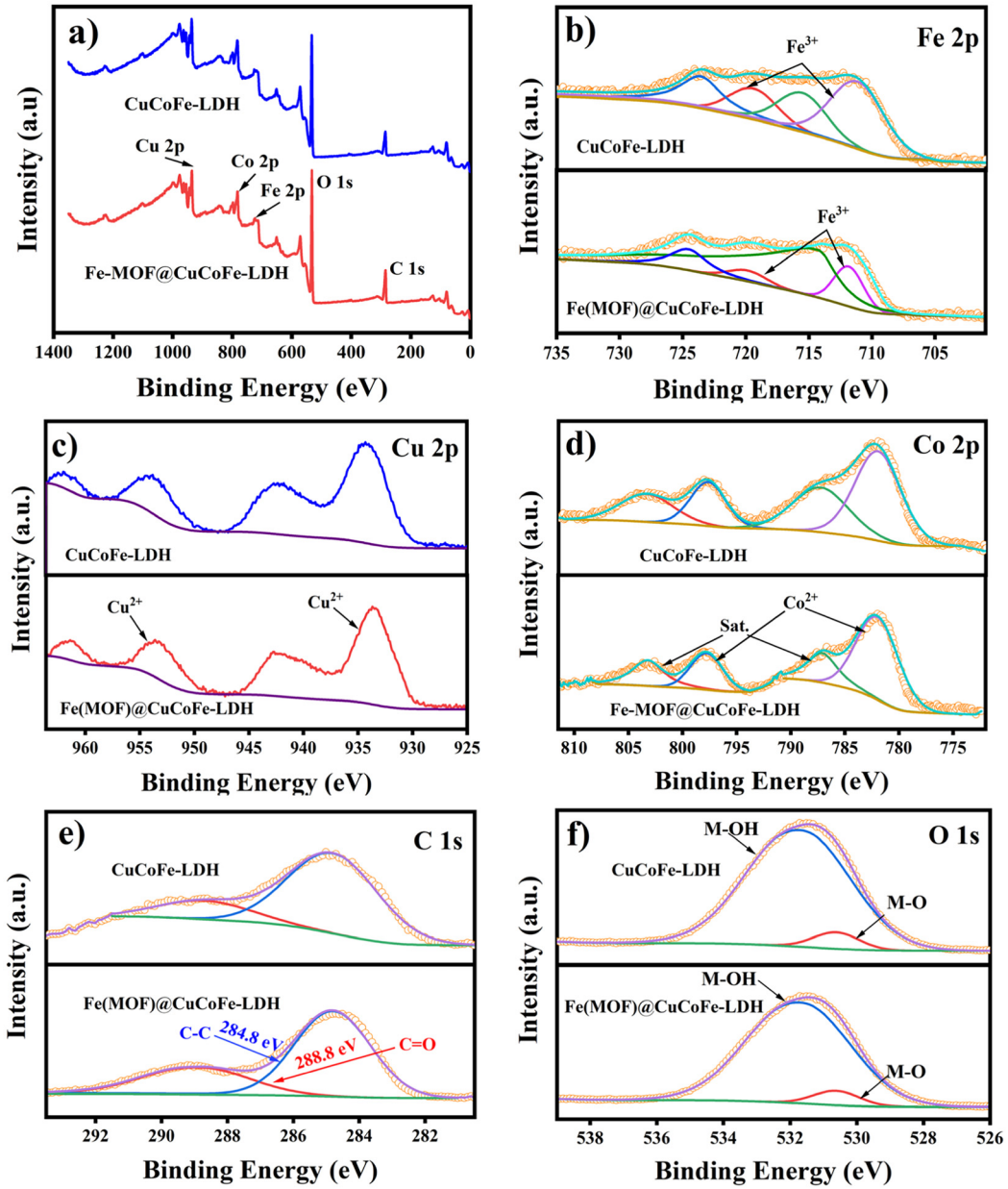

Fig. 4 XPS spectra of CuCoFe-LDH and Fe-MOF@CuCoFe-LDH. (a) Full scan, (b) Fe 2p spectra, (c) Cu 2p spectra, (d) Co 2p spectra, (e) C 1s spectra, and (f) O 1s spectra.

MOF@CuCoFe-LDH composite exhibited superior TC adsorption performance, which is attributed to the synergistic effects between the two components. SEM images (Fig. 2) reveal that Fe-MOF nanospheres (~100 nm) are uniformly hybridized into CuCoFe-LDH nanocluster flakes, forming a hierarchical heterostructure. This unique architecture effectively prevents the restacking of LDH nanosheets—a common issue in pristine LDH materials that reduces active site exposure. As observed in SEM images (Fig. 2b, c and d), pristine CuCoFe-LDH exhibits aggregated sheet-like structures with limited interlayer spacing, while the composite's Fe-MOF nanospheres act as "spacers" to separate LDH flakes, creating abundant interspaces for TC molecule diffusion. This structural optimization aligns with the layered "sandwich" structure design principle reported by Xu *et al.*,[51] where hierarchical architectures maximize mass transfer efficiency and active site accessibility. The clustered Fe-MOF and layered CuCoFe-LDH merge to create a complex microarchitecture, offering enhanced adsorption pathways and sites for TC molecules.[52] Additionally, XRD analysis (section 3.1) confirms that the composite has reduced crystallite size and increased microstrain compared to pristine CuCoFe-LDH, which further increases surface defect sites for TC binding. Moreover, the metal ion coordination in Fe-MOF complements the ion exchange capabilities of CuCoFe-LDH, enabling more comprehensive interactions with TC and boosting adsorption efficiency.[53]

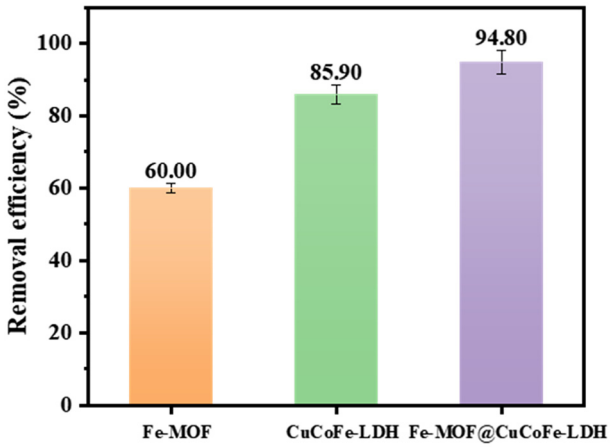

Fig. 5 Comparison of TC adsorption performance of different adsorbents (experimental conditions: $C_{adsorbent}$ = 0.2 g L^{-1}, T = 298 K, C_0 (TC) = 300 mg L^{-1}).

As confirmed by XPS analysis (section 3.4), the metal species in the composite exist as Cu(II), Co(II), and Fe(III). Fe (III) enhances the compatibility between the Fe-MOF and CuCoFe-LDH (benefiting from the environmental stability of Fe-based materials);[30] multi-metal species of Cu(II), Co(II), and Fe(III) strengthen coordination bonding with the electron-donating functional groups of TC molecules (*e.g.*, –OH and $–CONH_2$), electrostatic interaction with protonated TC species, and metal–π interaction with the aromatic rings of the TC molecular structure framework. Owing to its mass-transferred hierarchical architectures, the Fe-MOF@CuCoFe-LDH composite possesses abundant accessible metal-active sites. The synergy among these multi-metal sites enhances removal efficiency by promoting electron transfer,[26,38] thereby maximizing the adsorbent's performance. This demonstrates the vital influence of complex molecular interactions and synergetic effects on the overall adsorption process.

3.6 Adsorption kinetics

The time-dependent changes in the adsorption capacity of Fe-MOF@CuCoFe-LDH for TC are shown in Fig. 6a. The TC adsorption capacity of Fe-MOF@CuCoFe-LDH rose at a quick rate in the initial 45 min, then gradually increased to a maximum value at around 24 h, and then remained at a relatively constant level to reach adsorption equilibrium. To analyze the sorption kinetics of TC onto Fe-MOF@CuCoFe-LDH, the pseudo-first-order model (PFO, eqn (3)) and the pseudo-second-order model (PSO, eqn (4)) were applied to fit the experimental data for different contact times, and the results are shown, respectively, in Fig. 6b and c.

$$\ln(q_e - q_t) = \ln q_e - k_1 t \quad (3)$$

$$\frac{t}{q_t} = \frac{t}{q_e} + \frac{I}{(k_2 q_e^2)} \quad (4)$$

where k_1 (L mg^{-1}) and k_2 (mg g^{-1}) are, respectively, the constants of the PFO and PSO models.

As shown in Fig. 6b and c as well as Table 1 (the kinetics parameters), the PFO model exhibited poor correlation (R^2 = 0.7750), while the PSO model fits excellently with the experiment data (R^2 = 0.9994). The theoretical adsorption equilibrium capacity ($q_{e,cal}$) of 500.0 mg g^{-1} calculated using the PSO equation also closely matched the experimental value ($q_{e,exp}$) of 489.2 mg g^{-1}, indicating that the PSO model is suitable for describing the adsorption process, also demonstrating the dominance of chemisorption in it.[52] As shown in Table 1, the PSO rate constant of k_2 was 0.111 × 10^{-3} g (mg min)$^{-1}$, and the initial adsorption rate of h ($h = k_2 q_e^2$) was 27.78 mg (g

Table 1 Kinetics parameters for the adsorption of TC on Fe-MOF@CuCoFe-LDH

Kinetics models	Parameters	Fe-MOF@CuCoFe-LDH
Pseudo-first-order	$q_{e,exp}$ (mg g^{-1})	489.2
	$q_{e,cal}$ (mg g^{-1})	162.2
	$k_1 \times 10^{-3}$ (min^{-1})	3.563
	R^2	0.7750
Pseudo-second-order	$q_{e,\ cal}$ (mg g^{-1})	500.0
	$k_2 \times 10^{-3}$ (g (mg min)$^{-1}$)	0.111
	h (mg (g min)$^{-1}$)	27.78
	$t_{1/2}$ (min)	18
	R^2	0.9994

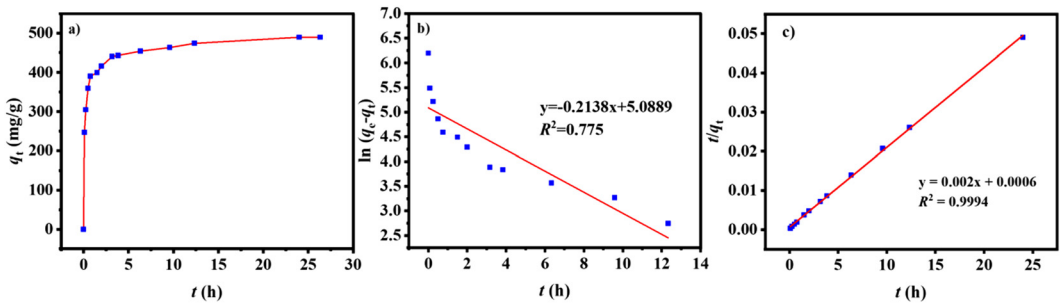

Fig. 6 The adsorption kinetics of TC on Fe-MOF@CuCoFe-LDH: (a) the effect of contact time on the adsorption capacity; (b) the pseudo-first-order model fitting plots; (c) the pseudo-second-order model fitting plots (experimental conditions: $C_{adsorbent}$ = 0.2 g L^{-1}, T = 298 K, C_0 (TC) = 100 mg L^{-1}).

min)$^{-1}$, confirming the fast adsorption process for the composite. Practically, the half-equilibrium time of $t_{1/2}$ ($t_{1/2} = 1/(k_2 q_e)$) was only 18 min, also demonstrating that TC adsorption on Fe-MOF@CuCoFe-LDH was rapid.

3.7 Adsorption isotherms

Adsorption isotherms (Fig. 7) were obtained by varying the TC initial concentration. The adsorption capacities increased with the decrease of the adsorbent dosage. Three isotherm models of Langmuir (eqn (5)), Freundlich (eqn (6)), and Temkin (eqn (7)) were used to interpret TC binding behavior.

$$\text{Langmuir isotherm equation}: \frac{C_e}{q_e} = \frac{C_e}{q_m} + \frac{1}{K_L q_m} \quad (5)$$

$$\text{Freundlich isotherm}: q_e = K_F C_e^{1/n_F} \quad (6)$$

$$\text{Temkin isotherm}: q_e = \frac{RT}{b}(\ln K_T C_e) \quad (7)$$

where q_m (mg g^{-1}) is the maximum adsorption capacity; K_L (L mg^{-1}), K_F (mg g^{-1}) and K_T (L mg^{-1}) are, respectively, the constants of Langmuir, Freundlich and Temkin; $1/n_F$ is a Freundlich constant indicative of the surface heterogeneity; and b is a Temkin constant related to sorption heat.

The Langmuir model provided the best fit to experimental data, as evidenced by higher R^2 values (0.9902–0.9935) compared to the Freundlich (0.8464–0.9472) and Temkin (0.9398–0.9779) models (Table 2). The Langmuir model assumes monolayer adsorption on a homogeneous surface, supported by the composite's uniform hierarchical structure (SEM images, Fig. 2c and d). Table 2 also presents isotherm parameters as well as the average percentage error (APE%). The Langmuir model exhibited the lowest APE% (6.27–8.94%), further confirming its superiority in describing the adsorption. The Langmuir maximum monolayer adsorption capacity of TC on Fe-MOF@CuCoFe-LDH was extremely high, 2500 mg g^{-1}. The Langmuir constant of K_L reflects the affinity of the adsorption, and the K_L values were 0.2083–0.5263, which are all between 0 and 1 under all three dosages, indicating the favorable adsorption for TC.[54,55] Furthermore, the Temkin model's relatively good R^2 and APE% indicate a relatively uniform binding energy distribution and the existence of strong intermolecular interaction between TC and Fe-MOF@CuCoFe-LDH. While, the Freundlich model's low R^2 values suggest minor surface heterogeneity, likely from the multi-metals' hybridity on the hierarchical architectures of the Fe-MOF@CuCoFe-LDH composite.[56]

Table 2 Isotherm parameters for the adsorption of TC on Fe-MOF@CuCoFe-LDH

Models	Parameters	0.5 g L^{-1}	0.2 g L^{-1}	0.1 g L^{-1}
Langmuir	q_m (mg g^{-1})	1000	2000	2500
	K_L (L mg^{-1})	0.5263	0.2083	0.3333
	APE%	7.39	8.94	6.27
	R^2	0.9935	0.9911	0.9902
Freundlich	K_F (mg g^{-1})	309.9	403.8	721.5
	$1/n_F$	0.6365	0.4245	0.3225
	APE%	10.39	21.08	13.37
	R^2	0.9472	0.8464	0.9031
Temkin	B	13.58	8.290	5.098
	K_T (L mg^{-1})	7.108	4.090	5.510
	APE%	10.28	11.82	7.920
	R^2	0.9680	0.9398	0.9779

3.8 Adsorption thermodynamics

Fig. 8a shows the adsorption capacity of TC on MOF@CuCoFe-LDH at three different temperatures. The progressive increase in adsorption capacity with rising temperature suggests an endothermic adsorption process, where elevated thermal energy enhances interactions between TC and the composite.[57] Fig. 8b shows the Vant Hoff equation (eqn (8)) fitting curve, which is used for the calculation of the adsorption thermodynamics. These thermodynamic measures can help us to understand the spontaneity, energy changes and disorder of the adsorption behavior, and help us to get good insights into the nature of the adsorption process under different thermal conditions. The thermodynamics parameters (calculated using eqn (8) and (9)) are listed in Table 3.

$$\ln K = \frac{\Delta S^0}{R} - \frac{\Delta H^0}{RT} \quad (8)$$

$$\Delta G^0 = -RT \ln K \quad (9)$$

where R (J (mol K)$^{-1}$) represents the ideal gas constant (8.314 J (mol K)$^{-1}$); T (K) represents the temperature, and ln$K = q_e/C_e$.

The negative values of ΔG^0 indicate that the adsorption of TC onto Fe-MOF@CuCoFe-LDH is spontaneous.[58] The slight

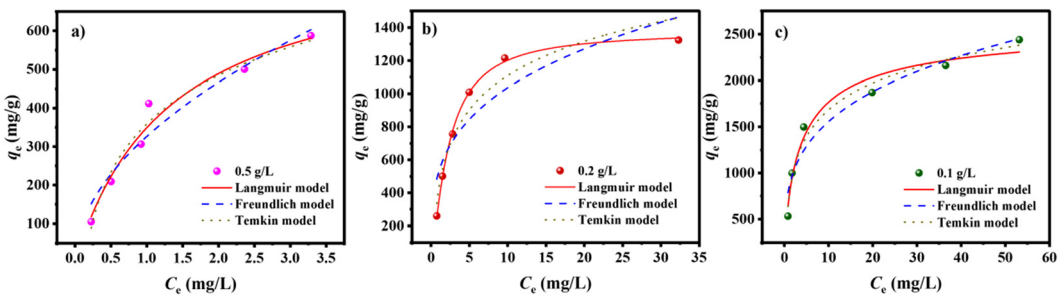

Fig. 7 The adsorption isotherms of TC on Fe-MOF@CuCoFe-LDH under different adsorbent dosages of (a) 0.5, (b) 0.2, and (c) 0.1 mg L^{-1} (experimental conditions: T = 298 K, C_0 (TC) = 50–300 mg L^{-1}).

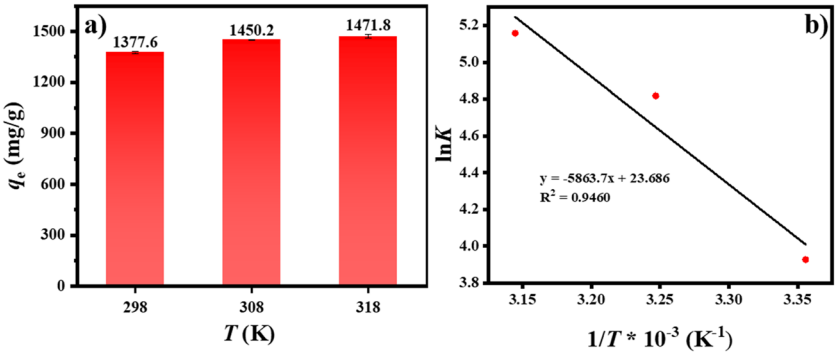

Fig. 8 Adsorption thermodynamics of TC on Fe-MOF@CuCoFe-LDH: (a) the effect of temperature on adsorption capacity; (b) Vant Hoff equation fitting curve (experimental conditions: $C_{adsorbent}$ = 0.2 g L^{-1}, T = 298, 308, 318 K).

Table 3 Thermodynamics parameters for the adsorption of TC on Fe-MOF@CuCoFe-LDH

		ΔG^0 (kJ mol^{-1})		
ΔH^0 (kJ mol^{-1})	ΔS^0 (J $(mol\ K)^{-1}$)	298 K	308 K	318 K
48.75	196.93	−9.73	−12.34	−13.64

reduction of ΔG^0 with temperature increase demonstrates that high temperatures increase the spontaneity of the adsorption. The positive ΔH^0 value indicates the endothermic nature of the TC adsorption on Fe-MOF@CuCoFe-LDH, which is in agreement with the observations presented in Fig. 8a. High temperature is more conducive to the adsorption process. In addition, the positive entropy change (ΔS^0) indicates that a higher level of randomness or disorder occurs at the solid–liquid interface.[59] All these thermodynamics results confirm the fact that the adsorption process is not only spontaneous, but also more favorable at a higher temperature.

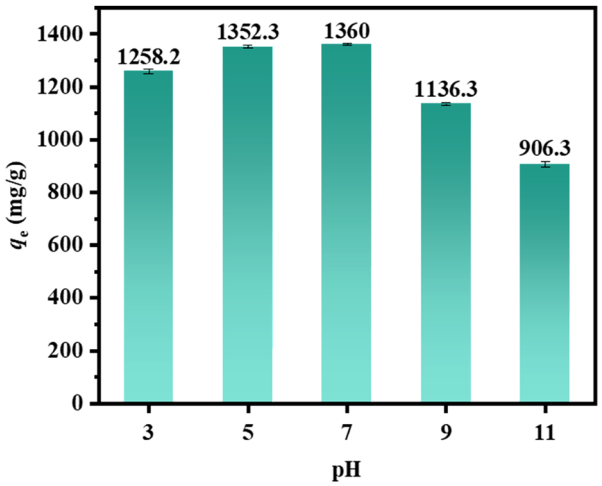

Fig. 9 The influence of pH on adsorption of TC on Fe-MOF@CuCoFe-LDH (experimental conditions: $C_{adsorbent}$ = 0.2 g L^{-1}, T = 298 K, C_0 (TC) = 300 mg L^{-1}).

3.9 Effect of pH

The effect of pH on TC adsorption by Fe-MOF@CuCoFe-LDH was analyzed under different pH conditions, and the results are exhibited in Fig. 9. The TC adsorption capacity on Fe-MOF@CuCoFe-LDH progressively increased from pH 3 to 7, reaching a maximum adsorption capacity of 1360 mg g^{-1} under neutral circumstances (pH 7). TC in aqueous solutions can exist as cation species of TCH_3^+ (pH < 3.3), zwitterion species of TCH_2^0 (3.3 < pH < 7.68), or anion species of TCH^- and TC^{2-} (pH > 7.68) due to protonation–deprotonation activities under different pH conditions.[60] Within the pH range of 5–7, TC exists in a neutral and uncharged state, and the adsorption capacity was relatively the highest. Some non-electrostatic interactions, primarily metal complexation and metal–π interactions, which are attributed to the multi-metal active site synergy on the composite surface, along with the hydrophobic effect between nearly uncharged TC molecules and the composite adsorbent, were the main attractive forces for the adsorption.[61,62] At pH 3, the relatively high adsorption capacity may be ascribed to the electrostatic attraction and H-bond interaction between protonated TC molecules and the adsorbent Fe-MOF@CuCoFe-LDH.[56] As pH increased from 7 to 11, the adsorbent's TC adsorption ability progressively declined. This is because, at pH > 8, TC was gradually negatively charged, and the strengthened electrostatic repulsion between TC and Fe-MOF@CuCoFe-LDH led to a decrease in the adsorption capacity.[58,63]

3.10 Adsorbent regeneration

Reusability represents a critical attribute of adsorbent materials, directly influencing their economic viability and environmental sustainability in water treatment applications. As demonstrated in Fig. 10, the Fe-MOF@CuCoFe-LDH composite exhibited excellent regeneration capability through a simple washing and drying procedure. Notably, it maintains a high TC removal efficiency of 97.8% even after five consecutive adsorption–desorption cycles, indicating its robust structural

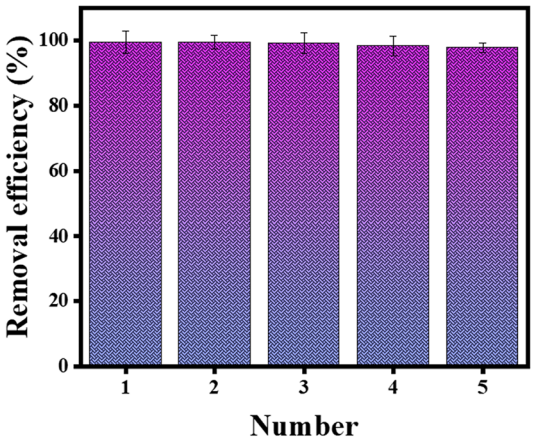

Fig. 10 Cycling performance of Fe-MOF@CuCoFe-LDH for the adsorption of TC (experimental conditions: $C_{adsorbent}$ = 1.0 g L^{-1}, T = 298 K, C_0 (TC) = 20 mg L^{-1}).

stability and operational durability. This high retention of performance reflects the strong potential of the Fe-MOF@CuCoFe-LDH composite for practical implementation. Material recycling significantly reduces operational costs and conserves resources. The development and utilization of the reusable Fe-MOF@CuCoFe-LDH adsorbent is expected to promote effective and sustainable pollution control.

4. Conclusion

The Fe-MOF was *in situ* modified onto ternary CuCoFe-LDH to fabricate a composite adsorbent of Fe-MOF@CuCoFe-LDH *via* a two-step hydrothermal synthesis method. SEM, XRD, FT-IR, and XPS characterization confirmed that Fe-MOF nanospheres were uniformly assembled and sandwiched between the layers of the CuCoFe-LDH flakes. The hierarchical architectures of Fe-MOF@CuCoFe-LDH enhanced the mass transfer efficiency and active site accessibility. The metals of copper and cobalt were present in the positive divalent state, whereas iron existed in the positive trivalent state. Resulting from the abundant available muti-metal active sites, MOF@CuCoFe-LDH exhibited extremely attractive adsorption performance with a Langmuir monolayer maximum adsorption capacity of 2500 mg g^{-1} to TC. Notably, a fast adsorption process was presented with a half-equilibrium time of only 18 min. The TC adsorption on MOF@CuCoFe-LDH was endothermic and spontaneous according to the thermodynamics analysis. The proposed adsorption mechanism includes metal complexation, metal–π interaction, hydrophobicity, H-bonding and electrostatic interactions. In addition, Fe-MOF@CuCoFe-LDH exhibited exceptional cycling stability for 5 cycles.

Conflicts of interest

There are no conflicts to declare.

Data availability

The authors confirm that the data supporting the findings of this study are available within the article.

Acknowledgements

This work was financially supported by the National Science Fund for Distinguished Young Scholars (22425808), the National Natural Science Foundation of China (22278426 and 22508419), the Key Program of the National Natural Science Foundation of China (22138011), the Carbon Neutrality Research Institute Fund (CNIF20240103), and the Science Foundation of China University of Petroleum, Beijing (2462022YJRC002 and 2462025BJRC002).

References

1 B. Wang, X. Gao, R. Qiu, Y. Chen, Y. Gao, G. Hu and D. Yu, *Chem. Eng. J.*, 2025, **505**, 159642.
2 M. Pan, R. Gao, S. Liang, X. Hu, M. Xie, W. Chen and S. Wang, *Chem. Eng. J.*, 2025, **517**, 164397.
3 Z. Hou, H. Lan, X. An, R. Liu, L. Yang, L. Liu, H. Liu and J. Qu, *Chem. Eng. J.*, 2024, **497**, 155055.
4 L. Ma, D. Li, X. Chen, H. Xu and Y. Tian, *J. Hazard. Mater.*, 2024, **474**, 134738.
5 Y. Dong, C. Yi, S. Yang, J. Wang, P. Chen, X. Liu, W. Du, S. Wang and B. F. Liu, *Nanoscale*, 2019, **11**(10), 4562–4570.
6 Y. Shi, X. Wang, C. Feng and S. Yang, *iScience*, 2024, **27**(2), 108952.
7 J. Bi, K. Bao, M. Zhao, Y. Zha, T. Chen, C. Huang and Z. Lv, *Appl. Surf. Sci.*, 2025, **688**, 162385.
8 J. T. d. Oliveira, L. R. d. C. Costa, G. D. Agnol and L. A. Féris, *Ind. Eng. Chem. Res.*, 2025, **64**(3), 1700–1711.
9 Y. He, D. B. Jiang, J. Chen, D. Y. Jiang and Y. X. Zhang, *J. Colloid Interface Sci.*, 2018, **510**, 207–220.
10 Y. Zhang, C. Xia, Z. Ma, Z. Shao, C. Dong, X. Zheng and Z. Meng, *Surf. Interfaces*, 2025, **58**, 105871.
11 Z. Liu, Y. Huang, D. Li, W. Zhang, K. Zhao and Y. Tang, *Diamond Relat. Mater.*, 2024, **149**, 111620.
12 J. Zhong, X. Yuan, J. Xiong, X. Wu and W. Lou, *Environ. Res.*, 2023, **226**, 115633.
13 X. Zhang, J. Hou, S. Zhang, T. Cai, S. Liu, W. Hu and Q. Zhang, *Biochar*, 2024, **6**(1), 12.
14 J. Wu, X. Chang, Y. Guo and N. Xia, *Dyes Pigm.*, 2024, **226**, 112137.
15 R. Fu, J. Liu, Y. Ma, H. Li, X. Hai, J. Niu, X. Guo and X. Di, *J. Hazard. Mater.*, 2025, **487**, 137143.
16 J. Wang, X. Li, Y. Fang, Q. Huang and Y. Wang, *Colloids Surf., A*, 2023, **666**, 131372.
17 Z. Guo, J. Meng, X. Li, X. Wang, Y. Li and L. Hu, *Sep. Purif. Technol.*, 2025, **363**, 132264.
18 Z. Jiao, Y. Zhou, X. Dai, J. Wu, Y. Chen, M. Wu, W. Yao, Y. Yuan, Z. Xie, Y. Ma, A. Andrej and L. Wu, *Corros. Sci.*, 2025, **248**, 112805.

19 J. Zhao, Y. Lu, D. B. Wu, Y. C. Qin, Y. Xie, Y. Guo, W. Raza, G. Luo, M. A. Mushtaq, Y. F. Wu, X. Mu, Y. Ling, T. Ilyas, Q. U. Hassan and C. M. Gao, *Sep. Purif. Technol.*, 2023, **305**, 122508.
20 D. A. Valdivieso-Vera and M. O. Guerrero-Pérez, *Catal. Today*, 2024, **442**, 114935.
21 F. L. Theiss, S. J. Couperthwaite, G. A. Ayoko and R. L. Frost, *J. Colloid Interface Sci.*, 2014, **417**, 356–368.
22 M. Ding, M. Li, Y. Wang and Z. Li, *Int. J. Hydrogen Energy*, 2025, **120**, 304–314.
23 S. Riaz, S. Ullah, S. Bashir, A. u. Rehman, R. Iqbal, T. Najam, M. A. Ismail, M. R. Karim, S. S. A. Shah and M. A. Nazir, *Appl. Clay Sci.*, 2025, **275**, 107866.
24 H. H. Kim, P. G. Koster van Groos, Y. Zhao and A. L. T. Pham, *Water Res.*, 2024, **260**, 121925.
25 S. Samuel, Z. Rezvani and A. R. Amani-Ghadim, *Environ. Prog. Sustainable Energy*, 2017, **36**(2), 372–381.
26 H. Y. Tian, Y. Li, M. Y. Xia, B. Y. Cui, C. Liu, X. H. Du, Z. H. Wang, X. Y. Duan and J. H. Cui, *Arabian J. Chem.*, 2024, **17**(3), 105645.
27 L. Lu, J. Bi, A. Shahab, H. Zhang, S. Rad and Z. Wu, *Environ. Technol. Innovation*, 2024, **34**, 103629.
28 S. Gai, J. Zhang, R. Fan, K. Xing, W. Chen, K. Zhu, X. Zheng, P. Wang, X. Fang and Y. Yang, *ACS Appl. Mater. Interfaces*, 2020, **12**(7), 8650–8662.
29 K. Shi, H. Su, K. Liu, Y. Zhang and J. Zhu, *Sep. Purif. Technol.*, 2025, **357**, 130155.
30 S. Li, F. Wu, R. Lin, J. Wang, C. Li, Z. Li, J. Jiang and Y. Xiong, *Chem. Eng. J.*, 2022, **429**, 132217.
31 Y. Yang, Z. Zheng, W. Ji, J. Xu and X. Zhang, *J. Hazard. Mater.*, 2020, **395**, 122686.
32 L. K. Njaramba, Y. Yoon and C. M. Park, *npj Clean Water*, 2024, **7**(1), 14.
33 R. Wang, H. Xu, K. Zhang, S. Wei and W. Deyong, *J. Hazard. Mater.*, 2019, **364**, 272–280.
34 Y. C. Zhao, H. W. Ma, J. D. Sun, J. H. Luo, Y. Su, L. Feng, T. Z. Liu, F. Q. Zhan, Z. Q. Yu, T. Yang, D. X. Liu and P. K. Liaw, *Rare Met.*, 2025, **44**(7), 4913–4935.
35 Y. Cai, J. Li, Q. Zhang, C. Liu, C. Wang, H. Shi, L. Jiang and D. Wu, *Sep. Purif. Technol.*, 2025, **376**, 134078.
36 Shehriyar, A. Khurram, A. Jabbar, M. A. Khan, W. Liu, S. Mutahir, A. Munir and S. I. Al-Saeedi, *Desalination*, 2026, **617**, 119438.
37 S. Mutahir, G. e. Rukhsar, A. Khurram, M. A. Khan, Z. E. Huma, Y. Qunhui and E. Alzahrani, *J. Ind. Eng. Chem.*, 2025, **154**, 806–821.
38 J. Y. Lu, Z. Q. Bu, Y. Q. Lei, D. Wang, B. He, J. Wang and W. T. Huang, *J. Mol. Liq.*, 2024, **409**, 125503.
39 T. Yang, J. Huang, Z. Liu and C. Chen, *Chem. Commun.*, 2025, **61**(62), 11681–11684.
40 X. Yang, J. Cheng, Y. Xu, H. Li, W. F. Tu and J. H. Zhou, *Chem. Eng. J.*, 2023, **472**, 145076.
41 H. Fu, X. X. Song, L. Wu, C. Zhao, P. Wang and C. C. Wang, *Mater. Res. Bull.*, 2020, **125**, 110806.
42 N. Liu, W. Huang, X. Zhang, L. Tang, L. Wang, Y. Wang and M. Wu, *Appl. Catal., B*, 2018, **221**, 119–128.
43 S. Ranjbari, B. Tanhaei, A. Ayati, S. Khadempir and M. Sillanpaa, *Int. J. Biol. Macromol.*, 2020, **155**, 421–429.
44 S. J. Xia, M. M. Shao, J. L. Xue and Z. M. Ni, *Chin. J. Inorg. Chem.*, 2016, **32**(6), 983–993.
45 J. Wang, S. Lei and L. Liang, *Appl. Surf. Sci.*, 2020, **530**, 147187.
46 Y. Wang, X. Wang, Y. Li, J. Li, F. Wang, S. Xia and J. Zhao, *Chem. Eng. J.*, 2020, **392**, 123808.
47 S. Mutahir, M. A. Khan, Y. Qunhui, S. Mehboob, M. Bououdina, S. M. Elkholi, A. Khan, R. A. Abumousa and M. Humayun, *J. Saudi Chem. Soc.*, 2024, **28**(2), 101821.
48 R. Liang, F. Jing, L. Shen, N. Qin and L. Wu, *J. Hazard. Mater.*, 2015, **287**, 364–372.
49 M. Rinawati, Y. X. Wang, K. Y. Chen and M. H. Yeh, *Chem. Eng. J.*, 2021, **423**, 130204.
50 H. Wang, D. Yong, S. Chen, S. Jiang, X. Zhang, W. Shao, Q. Zhang, W. Yan, B. Pan and Y. Xie, *J. Am. Chem. Soc.*, 2018, **140**(15), 5320.
51 H. Xu, Y. Wang, M. Liu and Y. Zhai, *ACS Appl. Mater. Interfaces*, 2025, **17**(33), 47679–47695.
52 G. Liu, J. Yang, Y. Zhao and X. Xu, *RSC Adv.*, 2022, **12**(7), 4408–4416.
53 J. Huang, Z. Zhang, Y. Wei, L. Guo, J. Liu, C. Zhang, Z. Xue and S. Sun, *Chem. Inorg. Mater.*, 2023, **1**, 100004.
54 S. Mutahir, S. Akram, M. A. Khan, H. S. Deng, A. M. Naglah, A. A. Almehizia, M. A. Al-Omar, F. I. Alrayes and M. S. Refat, *Chem. Eng. Sci.*, 2024, **283**, 119399.
55 S. Mutahir, M. A. Khan, H. Ishfaq, S. B. Ahmed, A. S. Abouzied, B. Huwaimel and H. Deng, *Biomass Convers. Biorefin.*, 2023, **14**(22), 29189–29200.
56 R. Liu, W. Ji, W. Wang, Y. Li, L. Yin, Y. Song and G. He, *Sep. Purif. Technol.*, 2025, **361**, 131349.
57 Y. Chao, W. Zhu, X. Wu, F. Hou, S. Xun, P. Wu, H. Ji, H. Xu and H. Li, *Chem. Eng. J.*, 2014, **243**, 60–67.
58 X. Liu, J. Luo, Y. Zhu, Y. Yang and S. Yang, *J. Alloys Compd.*, 2015, **648**, 986–993.
59 Q. Song, J. Liang, Y. Fang, C. Cao, Z. Liu, L. Li, Y. Huang, J. Lin and C. Tang, *J. Hazard. Mater.*, 2019, **364**, 654–662.
60 Y. Zhao, X. Gu, S. Gao, J. Geng and X. Wang, *Geoderma*, 2012, **183**, 12–18.
61 Z. Guo, F. Yang, R. Yang, L. Sun, Y. Li and J. Xu, *Sep. Purif. Technol.*, 2021, **274**, 118949.
62 L. C. Hsu, Y. T. Liu, C. H. Syu, M. H. Huang, Y. M. Tzou and H. Y. Teah, *R. Soc. Open Sci.*, 2018, **5**(3), 171941.
63 Y. Sun, Q. Yue, B. Gao, Q. Li, L. Huang, F. Yao and X. Xu, *J. Colloid Interface Sci.*, 2012, **368**, 521–527.
64 H. C. Fu, A. T. Zhang, F. H. Jin, H. W. Guo, W. J. Huang, W. T. Cheng and J. Q. Liu, *J. Colloid Interface Sci.*, 2022, **607**, 1269–1279.

